Incoherent Nature of M_2 Internal Tides at the Hawaiian Ridge

N. V. Zilberman

Scripps Institution of Oceanography, University of California, San Diego, La Jolla, California

M. A. Merrifield, G. S. Carter, and D. S. Luther

University of Hawaii at Manoa, Honolulu, Hawaii

M. D. Levine

Oregon State University, Corvallis, Oregon

T. J. Boyd

Scottish Association for Marine Science, Oban, United Kingdom

ABSTRACT

Moored current, temperature, and conductivity measurements are used to study the temporal variability of M_2 internal tide generation above the Kaena Ridge, between the Hawaiian islands of Oahu and Kauai. The energy conversion from the barotropic to baroclinic tide measured near the ridge crest varies by a factor of 2 over the 6-month mooring deployment (0.5–1.1 W m^{-2}). The energy flux measured just off the ridge undergoes a similar modulation as the ridge conversion. The energy conversion varies largely because of changes in the phase of the perturbation pressure, suggesting variable work done on remotely generated internal tides. During the mooring deployment, low-frequency current and stratification fluctuations occur on and off the ridge. Model simulations suggest that these variations are due to two mesoscale eddies that passed through the region. The impact of these eddies on low-mode internal tide propagation over the ridge crest is considered. It appears that eddy-related changes in stratification and perhaps cross-ridge current speed contribute to the observed phase variations in perturbation pressure and hence the variable conversion over the ridge.

1. Introduction

The generation of internal tides at ridges, seamounts, and island chains is an important energy pathway from the barotropic tide to mixing scales. The global distribution of deep-ocean internal tides has been examined with altimetric data, which has emphasized the time-independent or coherent (phase locked) component of the energetic M_2 semidiurnal tidal frequency (Ray and Mitchum 1998). In contrast, in situ measurements of internal tides typically highlight the sizeable time-dependent or incoherent fraction of the variability (Wunsch 1975). The incoherent nature of the internal tide develops in part because of interactions of the coherent internal tide with variable ocean currents (Rainville and Pinkel 2006b; Chavanne et al. 2010b) and the internal wave field (Alford et al. 2007). Alternatively, internal tide generation itself may vary with time because of changes in ocean stratification and currents at the generation site. Variable generation has been inferred from the time dependence of the internal tide energy flux near source regions (e.g., Eich et al. 2004); however, direct estimation of the barotropic to baroclinic conversion has received less attention. The intent of this paper is to compute directly time-variable internal tide generation at the Kaena Ridge (KR), Hawaii, using nearly full-depth moored observations and to show that factor of 2 changes in the M_2 internal tide generation occur, which we attribute to internal tide phase variations induced by mesoscale variability at the ridge.

In addition to a better understanding of the incoherent nature of internal tides, a motivation for this

Corresponding author address: Nathalie Zilberman, Scripps Institution of Oceanography, University of California, San Diego, 9500 Gilman Drive, La Jolla, CA 92093–0230.
E-mail: nzilberman@ucsd.edu

work is the need for improved parameterizations of barotropic to baroclinic tidal energy conversion for tide modeling and the specification of tide-induced mixing in general circulation models (Jayne and St. Laurent 2001; Simmons et al. 2004). Tidal energy conversion is a function of the stratification, height, and steepness of the topography where the transfer occurs and the amplitude of the barotropic velocity and its orientation relative to the topography. Incorporation of the conversion parameterization in numerical models has led to better agreement between tidal simulations and observations (Egbert et al. 1994; Egbert and Erofeeva 2002; Zaron and Egbert 2006); however, further refinements are needed to close the barotropic tidal energy budget. The time dependency of the energy conversion is not well understood.

Direct observations of variable tidal conversion have been made on the New Jersey shelf by Kelly and Nash (2010). They found strong modulation of tidal conversion locally depending on the amplitude and phase of remotely generated internal tides, which contribute a stochastic component to the conversion process. Time-dependent conversion has been examined in numerical models that simulate both the tidal forcing and the background circulation. Zaron et al. (2009) has shown that including mesoscale circulation in a data-assimilative model leads to a 25% decrease of the barotropic to baroclinic tidal energy conversion compared to runs where background circulation is not considered. Zaron et al. (2009) suggests that the energy conversion varies because of changes in the relationship between the currents and the pressure field due to interactions between internal tide and mesoscale currents.

The Kaena Ridge, located between the islands of Oahu and Kauai, is a major generation site for internal tides along the Hawaiian Ridge (Merrifield and Holloway 2002; Martin et al. 2006; Lee et al. 2006), and it was the main study site for the Hawaii Ocean Mixing Experiment (HOME). Numerical simulations (Carter et al. 2008) indicate that the main internal tide generation sites at the KR are located between the 1500- and 3000-m isobaths on both sides of the ridge. Observations (Martin et al. 2006; Nash et al. 2006; Rainville and Pinkel 2006a; Cole et al. 2009) and numerical simulations (Merrifield and Holloway 2002; Carter et al. 2008) document the upward and downward M_2 tidal beams radiating from these generation sites. Nash et al. (2006) find strong kinetic energy density and weak net energy flux for the internal tide over the ridge crest, consistent with a standing wave pattern due to the superposition of crossing tidal beams from either flank of the ridge.

Prior to HOME, studies indicated a low-frequency modulation of the M_2 internal tide emanating from the Hawaiian Ridge. Mitchum and Chiswell (2000) examined

inverted echo sounder (IES) measurements collected at station A Long-Term Oligotrophic Habitat Assessment (ALOHA) (Karl et al. 1996), the Hawaii Ocean Time-series (HOT) site located 100 km north of Oahu (22°45N, 158°W) and in the path of internal tides propagating northeastward from the KR. Computed dynamic height amplitudes showed 30% interannual variations between 1975 and 1995. Significant correlations between sea level variations from Hawaii tide gauges, which were treated as a proxy for pycnocline depth, and the variable internal tide amplitude at station ALOHA suggested that the magnitude of internal tide generation at the ridge varies with the variable stratification at generation sites.

Intra-annual variations of the M_2 internal tide generated at the KR were investigated by Chiswell (2002) using additional IES data between 1993 and 1995. Modulations over 2–4 months of the M_2 internal tide amplitude and phase at station ALOHA and at Kaena Point (western tip of Oahu) were detected. The amplitude varies by a factor of 2 at ALOHA and a factor of 1.5 at Kaena Point; the phase variation is more pronounced at ALOHA (17.7° standard deviation) than at Kaena Point (9.8°). Chiswell (2002) suggests that the modulation of the baroclinic tide amplitude and phase at station ALOHA results because of interactions between a coherent internal tide generated at Kaena Ridge and mesoscale variability just off the ridge. Direct observations of the mesoscale circulation were not available for confirmation.

As part of the HOME study, Rainville and Pinkel (2006b) use ray theory and altimetric observations to show that phase changes of low-mode internal tides 400 km from the ridge are consistent with internal tide refraction by mesoscale currents. Chavanne et al. (2010a) use high-frequency radar observations to show that the amplitude and phase of semidiurnal internal tide in the near field of the ridge (within tens of kilometers) vary over the 6-month radar deployment. They conclude that the modulation is a result of refraction of the internal tide by mesoscale currents observed by the radars, confirming the hypothesis of Chiswell (2002). These studies pertain to the time-dependent refraction of coherent internal tides forming incoherent signals. The extent to which the generation at the Kaena Ridge itself is time variable (i.e., the hypothesis of Mitchum and Chiswell 2000) has not been evaluated with direct observations.

In this paper, we estimate time-variable M_2 internal tide generation using a mooring with nearly full-depth coverage at a generation site on the south side of the ridge. We present time series of the baroclinic conversion and energy flux for the M_2 tide at the KR obtained between December 2002 and May 2003 during the near-field
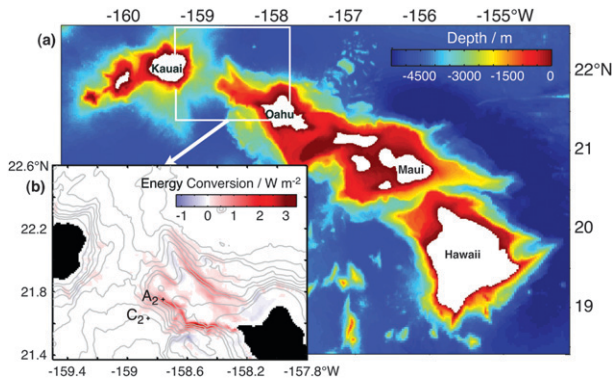
FIG. 1. (a) The multibeam bathymetry data for the KR. (b) The barotropic to baroclinic energy conversion predicted over the KR using the POM. Contour interval is 500 m.

phase of HOME. Variations in the local generation are related primarily to changes in the phase of the perturbation pressure, which suggests variations in the arrival time of internal tides generated on the north side of the ridge. We examine how the mesoscale circulation over the KR may affect the M_2 propagation speed over the ridge and hence the phase of the M_2 perturbation pressure, which is key to understanding modulations of the barotropic to baroclinic energy conversion rate.

We first describe the observations and model outputs used in this study (section 2). The technique for determining the M_2 barotropic and baroclinic tidal signals over 28-day windows is presented (section 3). Our main result is the computation of variable M_2 energy conversion from observations on the ridge (A2 mooring), which appears to match the observed variation in the M_2 energy flux off the ridge (C2 mooring) (section 4). Observed low-frequency variations in currents and stratification are related to two mesoscale eddy events described using a regional circulation model (section 5). We consider the extent to which internal tide generation is affected by changes in local stratification, as well the influence of mesoscale stratification and current changes on the internal tide phase speed. We believe that the mesoscale stratification and current changes affect the phase of the perturbation pressure, which contribute to the variable conversion (section 6). We conclude with a summary and discussion (section 7).

2. Observations and model simulations

a. Moored observations

The A2 subsurface mooring was deployed at 1331-m water depth on the south side of Kaena Ridge (21°45.087N, 158°45.522W) (Fig. 1). A2 is situated within an internal tide generation zone predicted by the Princeton Ocean

Model (POM) simulation of Carter et al. (2008). The C2 subsurface mooring was located in deep water (4010-m depth) 16.8 km southwest of A2 (21°37.850N, 158°51.609W). C2 is within the path of energetic internal tides propagating southwestward away from the KR in the POM simulation. The moorings were deployed from December 2002 through May 2003.

Temperature [Sea-Bird Electronics (SBE) 39 and miniature temperature recorders (MTRs)] and temperature–conductivity (SBE 37 and SBE 16) recorders were deployed between 210- and 1320-m depths at the A2 mooring and between 200- and 4000-m depths at the C2 mooring (for a description of the data, see Boyd et al. 2005). The sampling periods were 8 (SBE 16 and MTR), 6 (SBE 37), and 5 min (SBE 39) at the A2 mooring and 10 (SBE 16) and 5 min (SBE 37 and SBE 39) at the C2 mooring (Table 2).

Salinity is computed from temperature and conductivity following Fofonoff and Millard (1983). In the absence of conductivity measurements, salinity is inferred from temperature using the temperature–salinity (T–S) relationship obtained from directly measured temperature and conductivity (SBE 16 and SBE 37). A T–S relationship was not sampled below 900-m depth at the C2 mooring. At these depths, salinity is inferred using a T–S relationship obtained from CTD profiles at station ALOHA between December 2002 and May 2003. In the Hawaii region, interleaving of Antarctic Intermediate Water and North Pacific Intermediate Water can lead to T–S anomalies (Kennan and Lukas 1996); however, intrusion anomalies were not apparent in the A2 and C2 T–S plots.

Velocity time series were obtained at the A2 and C2 moorings using upward-looking acoustic Doppler current profilers (ADCPs) (Boyd et al. 2005). Three ADCPs mounted on the A2 mooring measured velocities nominally between 10- and 1288-m depths (Table 1). A 300-kHz ADCP placed at 99-m depth recorded velocities between 4- and 92-m depths, and two 75-kHz ADCPs, placed at 746- and 1306-m depths, recorded velocities in depth ranges of 160–730 m and 730–1300 m. The ADCPs at the A2 mooring recorded current velocity profiles with 20- (300 kHz) and 16-min (75 kHz) sampling intervals and 4- (300 kHz) or 8-m (75 kHz) vertical resolution. Two ADCPs mounted on the C2 mooring measured velocities between 10- and 720-m depths (Table 2). A 300-kHz ADCP placed at 92-m depth recorded velocities between 4 and 80 m, and a 75-kHz ADCP placed at 743-m depth recorded velocities between 200 and 720 m. The ADCPs at the C2 mooring recorded current speed and direction profiles with 20- (300 kHz) and 10-min (75 kHz) sampling interval and 4- (300 kHz) and 8-m (75 kHz) vertical resolution. The range of the ADCPs

TABLE 1. Instrumentation at the A2 mooring. The plus signs indicate the variable was measured by the instruments.

Instrument	Depth (m)	Temperature	Conductivity	Velocity
CTD HOT	0–200	+	+	
ADCP300	4–92			+
SBE 37	215	+	+	
SBE 37	223	+	+	
SBE 37	354	+	+	
SBE 16	362	+	+	
SBE 37	370	+	+	
SBE 37	459	+	+	
SBE 16	467	+	+	
SBE 37	475	+	+	
SBE 37	483	+	+	
SBE 16	491	+	+	
SBE 16	667	+	+	
SBE 39	675	+		
SBE 16	683	+	+	
SBE 39	691	+		
SBE 39	707	+		
SBE 16	715	+		
ADCP75	160–730			+
MTR	803	+		
SBE 39	883	+		
SBE 16	963	+	+	
SBE 39	979	+		
SBE 39	995	+		
SBE 39	1011	+		
SBE 39	1019	+		
SBE 16	1027	+	+	
SBE 39	1059	+		
SBE 37	1091	+	+	
SBE 39	1107	+		
SBE 39	1123	+		
SBE 39	1139	+		
SBE 16	1155	+	+	
SBE 39	1187	+		
SBE 37	1219	+	+	
SBE 39	1251	+		
SBE 39	1267	+		
SBE 39	1275	+		
SBE 37	1283	+	+	
ADCP75	730–1300			+
MTR	1318	+		
MTR	1323	+		

TABLE 2. Instrumentation at the C2 mooring. The plus signs indicate the variable was measured by the instruments.

Instrument	Depth (m)	Temperature	Conductivity	Velocity
CTD HOT	0–200	+	+	
ADCP300	4–80			+
SBE 16	202	+	+	
SBE 39	210	+		
SBE 37	342	+	+	
SBE 39	350	+		
SBE 37	453	+	+	
SBE 39	461	+		
SBE 16	477	+	+	
SBE 16	669	+	+	
SBE 37	677	+	+	
SBE 39	685	+		
SBE 37	693	+	+	
SBE 16	709	+	+	
ADCP75	200–720	+		+
SBE 16	867	+	+	
SBE 39	1067	+		
SBE 39	1265	+		
SBE 39	1765	+		
SBE 39	2274	+		
SBE 39	2855	+		
SBE 39	2863	+		
SBE 39	2871	+		
SBE 39	2879	+		
SBE 39	3386	+		
SBE 39	3459	+		
SBE 39	3467	+		
SBE 39	3475	+		
SBE 39	3483	+		
SBE 39	3491	+		
SBE 39	3997	+		

varied with effective acoustic scattering strength. Data used were limited to depths with at least 50% good pings per ensemble average.

b. CTD observations

Shipboard CTD profiles collected at station ALOHA were used to complement the A2 and C2 mooring observations, which were limited to depths greater than 200 m. Temperature profiles averaged between December and May over 15 yr in the upper 200 m at station ALOHA were used in a linear regression analysis to compute the depth profiles of the temperature in the upper 200 m based on the temperature measured at 200-m depth at each mooring. The inferred temperature profiles were used to extrapolate the A2 and C2 temperature time series at 200 m to the surface. We employed the same method to infer the time series of the salinity at 200 m to the surface at the A2 and C2 moorings using the salinity profiles collected at station ALOHA.

c. Princeton Ocean Model

The observed estimates of the time-dependent M_2 baroclinic tide energy flux and conversion are compared with numerical simulations from the Princeton Ocean Model. The POM simulations are described in detail in Carter et al. (2008). Briefly, POM is a hydrostatic, three-dimensional primitive equation model with sigma coordinates (Blumberg and Mellor 1987). The study grid has 0.01° (~1 km) horizontal resolution over an area 19°21′–22°26′N, 160°–156°W and progressively expands to 0.03° near the boundaries. A total of 61 vertical sigma levels are used distributed linearly with depth. The stratification, taken as uniform in the horizontal, is obtained using temperature and salinity profiles averaged between December 2002 and May 2003 from station ALOHA

(in the upper 200 m and below 1300 m) and the A2 mooring (between 200 and 1300 m). The turbulent energy equation is resolved using the Mellor and Yamada (1982) level-2.5 turbulence closure scheme (MY2.5).

POM is forced at each boundary with the M_2 tidal elevations and barotropic velocities provided by the inverse Ocean Topography Experiment (TOPEX)/Poseidon global tidal model 6.2 (TPXO6.2) of Egbert and Erofeeva (2002). A Flather boundary condition is used on the elevation and barotropic velocity at the four open boundaries, and a relaxation layer is applied to the baroclinic velocity and isopycnal displacement (Carter and Merrifield 2007). Each simulation has duration of 18 M_2 tidal cycles with the boundary forcing increased from zero to full strength over 1.3 days. The M_2 current amplitudes and phases are obtained from a harmonic fit over the last six tidal cycles of model output.

d. Navy Coastal Ocean Model

We compare simulations of subinertial currents from the Navy Coastal Ocean Model (NCOM) with the current observations at A2 and C2. NCOM is hydrostatic, Boussinesq, free-surface ocean model with 40 combined sigma/z-level coordinates and a horizontal spacing of $1/8°$ (Barron et al. 2006). The model is forced using wind stress from the Navy Operational Global Atmospheric Prediction System (NOGAPS). Net shortwave and longwave radiation at the sea surface and air temperature and air mixing ratio at 10 m above the sea surface are specified using the $1/8°$ global Modular Ocean Data Assimilation System (MODAS).

3. The time-variable M_2 tide

Observed temporal variations of the M_2 tide are assessed using a complex demodulation of the horizontal current and density measurements. Following Emery and Thomson (2001), a least squares fit of M_2, S_2, and N_2 harmonics is applied over a sliding 28-day window. A period of 28 days allows the separation of the M_2 and N_2 harmonics by the Rayleigh criterion. For data with gaps due to low acoustic backscatter at far range, we compute the complex demodulation if we have at least 120 profiles over the 28-day window with a minimum of 4 h between profiles. For comparison, the criterion for a reliable fit developed by Nash et al. (2006) using HOME profile data was 24 profiles irregularly spaced over 30 days with at least 3 h between profiles. For each 28-day window, the complex amplitude of the M_2 horizontal velocity is denoted by $\hat{\mathbf{u}}(z) = [\hat{u}(z), \hat{v}(z)]$, where $\hat{u}(z)$ and $\hat{v}(z)$ are the meridional and zonal components. The M_2, barotropic, horizontal velocity is estimated as

$$\hat{\mathbf{u}}_{\mathrm{bt}} = \frac{1}{H}\int_{-H}^{0}\hat{\mathbf{u}}(z)\,dz, \tag{1}$$

where H is the water depth. The complex amplitude of the M_2, baroclinic, horizontal velocity is

$$\hat{\mathbf{u}}'(z) = \hat{\mathbf{u}}(z) - \hat{\mathbf{u}}_{\mathrm{bt}}. \tag{2}$$

For each 28-day window, the complex amplitude of the M_2 density variation is denoted by $\hat{\rho}(z)$. The M_2 vertical displacement is computed as

$$\hat{\eta}(z) = \frac{g\hat{\rho}(z)}{\rho_0 N_B^2(z)}, \tag{3}$$

where ρ_0 is the reference density, g is the gravitational acceleration, and $N_B(z)$ is the background stratification computed as the stratification averaged over the 28-day window.

The barotropic vertical displacement associated with tidal flow over topography is estimated as

$$\hat{\eta}_{\mathrm{bt}}(z) = \frac{-i\hat{w}_{\mathrm{bt}}(z)}{\omega}, \tag{4}$$

where $\omega = 1.41 \times 10^{-4}$ rad s^{-1} is the M_2 frequency and $\hat{w}_{\mathrm{bt}}(z)$ is the barotropic vertical velocity, which is taken to vary linearly with depth from $\hat{w}_{\mathrm{bt}}(-H) = -\hat{\mathbf{u}}_{\mathrm{bt}} \cdot \nabla H$ at the bottom to $\hat{w}_{bt}(0) = 0$ at the surface.

The complex amplitude of the baroclinic vertical displacement is

$$\hat{\eta}'(z) = \hat{\eta}(z) - \hat{\eta}_{\mathrm{bt}}(z). \tag{5}$$

Following Kunze et al. (2002), the complex amplitude of the M_2 perturbation pressure is computed from $\hat{\eta}'(z)$ assuming the hydrostatic balance and that the depth-average perturbation pressure is zero,

$$\hat{p}'(z) = \int_{z}^{0} N_B^2(z')\hat{\eta}'(z')\,dz' \\ - \frac{1}{H}\int_{-H}^{0}\int_{z}^{0} N_B^2(z')\hat{\eta}'(z')\,dz'\,dz. \tag{6}$$

We consider a decomposition of the horizontal velocity $\hat{\mathbf{u}}$ and vertical displacement $\hat{\eta}$ in terms of dynamical modes,

$$\hat{\mathbf{u}}(z) = \sum_{n=0}^{4} p_n(z)\tilde{\mathbf{u}}_n \quad \text{and} \tag{7}$$

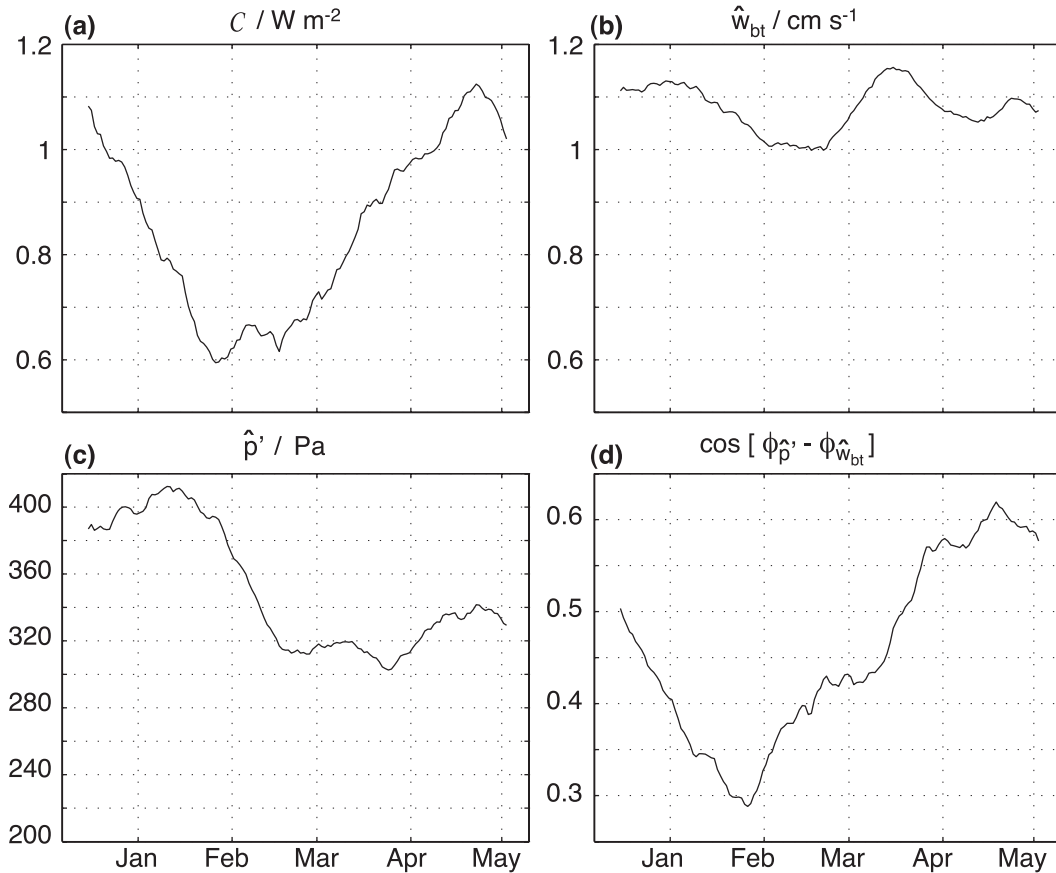$$\hat{\eta}(z) = \sum_{n=0}^{4} h_n(z)\tilde{\eta}_n,$$

FIG. 2. Barotropic to baroclinic energy conversion $\mathcal{C}$, barotropic vertical velocity amplitude $\hat{w}_{bt}$, perturbation pressure amplitude $\hat{p}'$, and cosine of the phase difference between the perturbation pressure and the barotropic vertical velocity $\cos(\phi_{\hat{p}'} - \phi_{\hat{w}_{bt}})$ for the M_2 tide observed at the A2 mooring.

where $p_n(z)$ is the vertical structure of the nth horizontal velocity, $h_n(z)$ is the vertical structure of the vertical displacement, and $\tilde{\mathbf{u}}_n$ and $\tilde{\eta}_n$ are the current and displacement amplitudes of the barotropic ($n = 0$) and baroclinic modes ($n \geq 1$) modes. Here, $h_n(z)$ and corresponding modal phase velocities c_n are estimated using the matrix eigenvalue method of Chelton et al. (1998) on a vertical grid with uniform 20-m spacing. The vertical resolution of the measurements at the A2 mooring (Table 1) only allows the first four baroclinic modes to be fitted with confidence.

4. M_2 energy conversion at the A2 mooring

The barotropic to baroclinic tidal energy conversion, or the rate of work done by the barotropic tide on the baroclinic tide, is computed as in Zilberman et al. (2009),

$$\mathcal{C} = \frac{1}{2}\mathrm{Re}[\hat{p}'(-H)\hat{w}_{bt}(-H)] \cdot (\mathrm{W\,m}^{-2}). \quad (8)$$

In terms of the M_2 amplitudes and Greenwich phases ($\phi_{p'}$ and $\phi_{w_{bt}}$) of $\hat{p}'(-H)$ and $\hat{w}_{bt}(-H)$, the energy conversion (8) becomes

$$\mathcal{C} = \frac{1}{2}|\hat{p}'(-H)||\hat{w}_{bt}(-H)|\cos(\phi_{\hat{p}'} - \phi_{\hat{w}_{bt}}). \quad (9)$$

Similarly, the energy conversion for modes 1–4 is calculated as in (8),

$$\mathcal{C}_n = \frac{1}{2}\mathrm{Re}[p_n'(-H)\hat{w}_{bt}(-H)]. \quad (10)$$

The model perturbation pressure p_n' is derived from (6), replacing $\hat{\eta}'$ with $h_n(z)\tilde{\eta}_n$. The modal conversion can be expressed in terms of the amplitudes and phases of $p_n'(-H)$ and $w_{bt}(-H)$ following (8).

Using Eq. (8), we compute the barotropic to baroclinic energy conversion at the A2 mooring for each 28-day window. The time variability of the energy conversion is characterized by a decrease from December to the end of January and an increase from February to April (Fig. 2a).

TABLE 3. Time-averaged barotropic to baroclinic energy conversion C_n and ratio of C_n relative to C computed at the A2 mooring.

Wave number bandwidth	Energy conversion (W m^{-2})	Energy conversion Ratio (%)
Mode 1	0.28	33
Mode 2	0.12	14
Mode 3	0.07	8
Mode 4	0.05	6
Modes 1–4	0.52	61

The conversion varies by nearly a factor of 2 between the largest values (1–1.1 W m^{-2}) in December and April and lowest values (0.6–0.7 W m^{-2}) at the end of January (Fig. 2a). The energy conversion averaged over the entire deployment is 0.85 W m^{-2}. For comparison, the POM conversion rate at the location of the A2 mooring is 1.03 W m^{-2}.

In terms of the contributions to the conversion described in (9), the amplitude (Fig. 2b) and phase (not shown) of w_{bt} remain nearly constant over time as expected for the barotropic tide. In contrast, the amplitude (Fig. 2c) and phase (Fig. 2d) of $\hat{p}'(-H)$ vary with time. The amplitude of $p'(-H)$ is high during the first conversion maximum at the start of the record but low during the conversion maxima at the end of the record. The time dependence of $p'(-H)$ phase, depicted in Fig. 2d as $\cos(\phi_{p'} - \phi_{w_{bt}})$, is similar in character to C, particularly the factor of 2 increase at the end of the record (Fig. 2a).

For local internal tide generation at the A2 site, we would expect the phase of $\hat{p}'(-H)$ to match $w_{bt}(-H)$. However, because the baroclinic energy propagates in both cross-ridge directions (Merrifield and Holloway 2002; Nash et al. 2006), the phase of $\hat{p}'(-H)$ at the internal tide generation sites is affected by remotely generated internal tides and hence does not match $w_{bt}(-H)$.

We next examine the composition of the energy conversion in terms of the baroclinic modes [Eq. (10)]. About 61% of the energy conversion is accounted for by the first four baroclinic modes, with 33% associated with mode 1 and 14% associated with mode 2 (Table 3). The energy conversions for modes 1 and 2 (Figs. 3a,b) vary in time similar to the total conversion, with a minimum in late January/early February (Fig. 2a). In terms of the contributions to the conversion, the amplitudes of $\hat{p}'_n(-H)$ for modes 1 and 2 are fairly constant (Figs. 3c,d) compared to the variation of the conversion (Figs. 3a,b). In contrast, we find that the phases (Figs. 3e,f) of $\hat{p}'_n(-H)$ for modes 1 and 2 exhibit a similar time dependence as the modal conversion (Figs. 3a,b). The magnitude of $\cos(\phi_{\hat{p}'} - \phi_{\hat{w}_{bt}})$ for mode 2 is larger than for mode 1 (Figs. 3e,f). The time variation in the phase

of $\hat{p}'_n(-H)$ leads to larger changes in $\cos(\phi_{\hat{p}'_n} - \phi_{\hat{w}_{bt}})$ for mode 2 (± 0.2) compared to mode 1 (± 0.1).

5. M_2 energy flux at the A2 and C2 moorings

The horizontal component of the depth-integrated baroclinic energy flux is

$$\mathbf{E} = \int_{-H}^{0} \frac{1}{2} \mathrm{Re}[\hat{p}'(z)\hat{\mathbf{u}}'(z)]\, dz. \qquad (11)$$

Similarly, the horizontal baroclinic energy flux for each mode is

$$\mathbf{E}_n = \int_{-H}^{0} \frac{1}{2} \mathrm{Re}[\hat{p}'_n(z)\hat{\mathbf{u}}'_n(z)]\, dz. \qquad (12)$$

The amplitude of $\mathbf{E}$ at the A2 mooring exhibits a low-frequency modulation, with a factor of 2 change between the largest values (>6000 W m^{-1}) in January and lowest values (<3500 W m^{-1}) from the end of February to May (Fig. 4a). Here, $\mathbf{E}$ is directed southwestward at A2 (Fig. 4c), with the time-averaged flux directed toward 239°. The amplitude of the time-averaged flux at A2 from POM (4511 W m^{-1}) is in good agreement with the observations (4080 W m^{-1}) and with observations by Nash et al. (2006) (4000 W m^{-1}) 20 km east from the A2 mooring (their station 3), at similar depth. The orientation of the time-averaged flux at A2 from POM (215°) is similar to the observed flux.

The fits to dynamical modes indicate that 92% of the energy flux is carried by the first two baroclinic modes, similar to the results of Nash et al. (2006). The magnitude and orientation of $\mathbf{E}_1$ differ over time compared to $\mathbf{E}_2$ (Fig. 5), implying a superposition of internal tides from different sources: that is, not just one tidal beam crossing the mooring.

The baroclinic energy flux at the C2 mooring is computed from Eq. (11), except the depth integral is over the upper 720-m-depth range rather than the full water depth. This is due to the lack of direct current measurements below 720 m. The energy flux exhibits a low-frequency modulation, with a factor of 2 change in amplitude between the largest values (>6000 W m^{-1}) in December and April and lowest values (<3500 W m^{-1}) at the end of January (Fig. 4b). The time-averaged baroclinic energy flux radiates away from the KR (190°), (Fig. 4d). The amplitude of the time-averaged flux from POM (2847 W m^{-1}) is lower than observed in the upper 720 m (4956 W m^{-1}) and is directed more normal to the ridge axis (220°). We note that far-field energy fluxes may exhibit substantial variation in space because of the superposition of waves from multiple generation sources
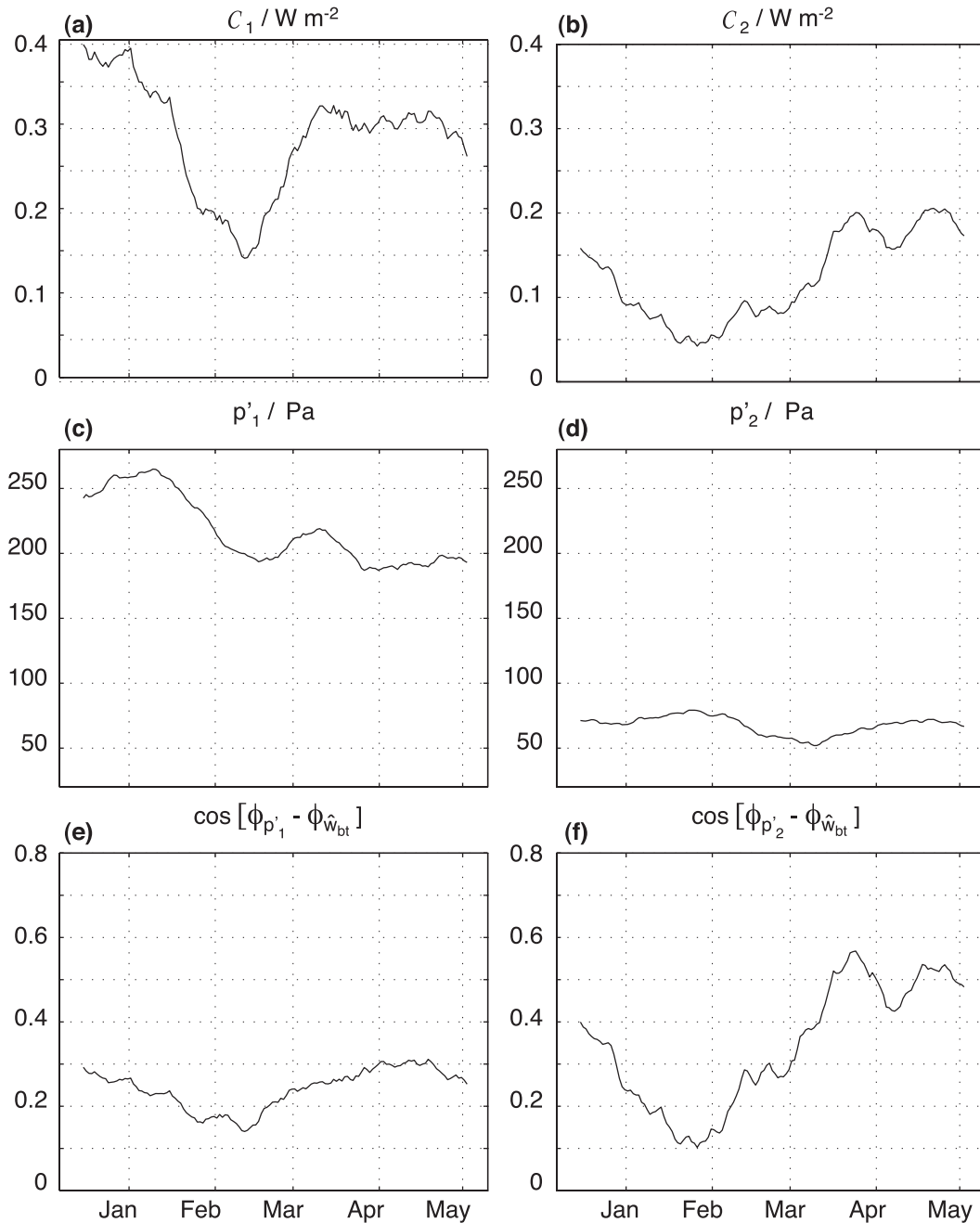
FIG. 3. Barotropic to baroclinic energy conversion $\mathcal{C}_n$, perturbation pressure amplitude p'_n, and cosine of the phase difference between the perturbation pressure and the barotropic vertical velocity $\cos(\phi_{p'_n} - \phi_{\hat{w}_{bt}})$, for baroclinic mode 1 ($n = 1$) and mode 2 ($n = 2$) for the M_2 tide observed at the A2 mooring.

(Rainville et al. 2010), as well as from potential interaction with offshore currents (Chavanne et al. 2010b). This may account for the poorer correspondence between model and observed energy flux at C2 compared to A2.

The time variability of the energy conversion at A2 (Fig. 4e) is similar to the flux in the upper water column

at C2 but is not related to the flux at A2. Our interpretation is that the A2 mooring is located at the shallow end of the conversion zone on the southern flank of the KR (Fig. 1a). Although M_2 baroclinic energy propagates in both cross-ridge directions at the Kaena Ridge (Merrifield and Holloway 2002; Nash et al. 2006), the southwestward net flux indicates that the dominant
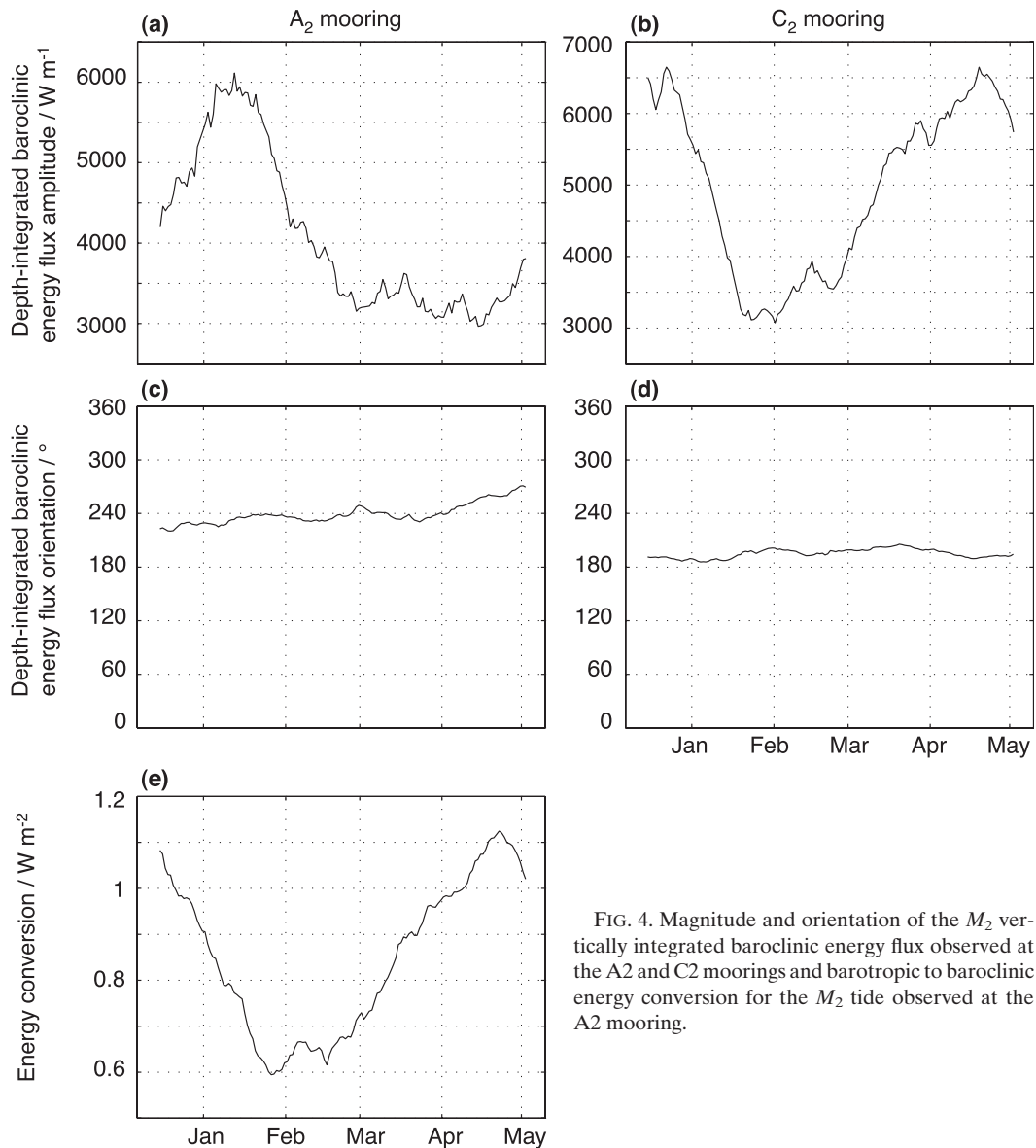
FIG. 4. Magnitude and orientation of the M_2 vertically integrated baroclinic energy flux observed at the A2 and C2 moorings and barotropic to baroclinic energy conversion for the M_2 tide observed at the A2 mooring.

source of internal tides at A2 is to the northeast of the site along the northern flank of the KR (Fig. 1b). Given that the net flux is to the southwest at A2, the main source of the energy flux must be from conversion zones on the northern flank; hence, the variability of the depth-integrated baroclinic energy flux at A2 does not necessarily have to match the conversion at A2 given all the factors that can influence the remotely generated flux by the time it reaches A2 (i.e., variable conversion on the north flank and interactions with currents over the ridge). The correspondence between the C2 flux and the A2 conversion suggests that the conversion on the south flank modifies the outgoing flux as observed at A2. Assuming that the conversion over the deep south flank of

the ridge covaries with the conversion at A2, then the radiated energy leaving the ridge (at C2) is likely to resemble the time variability of the south flank conversion (at A2).

6. Mesoscale circulation and variable M_2 conversion

Previous studies of semidiurnal internal tides at Hawaii suggest that the time variability of the tidal amplitude and phase is due to variable conversion because of changes in the background stratification at the generation sites (Mitchum and Chiswell 2000) and/or interactions between the propagating internal tide and
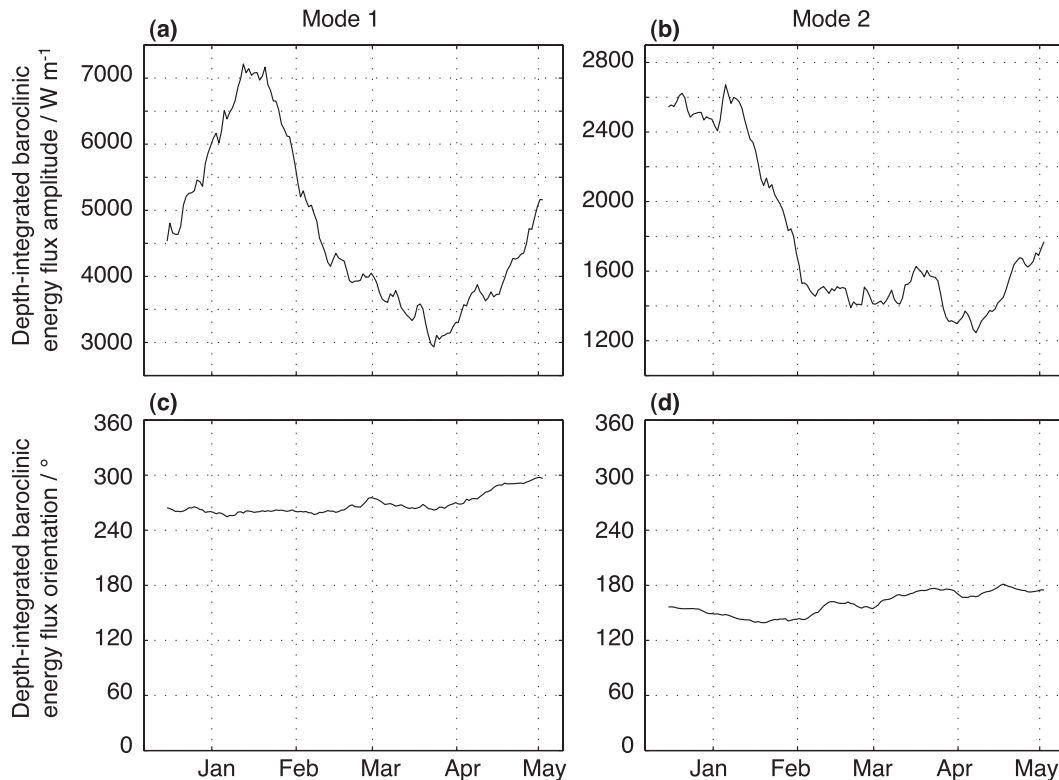
FIG. 5. Magnitude and orientation of the M_2 vertically integrated baroclinic energy flux for modes 1 and 2 observed at the A2 mooring.

mesoscale variability (Chiswell 2002; Chavanne et al. 2010b). In section 4, we found that the time variability of the barotropic to baroclinic energy conversion is affected primarily by the phase of $p'(-H)$. Modal decompositions suggest that a significant portion of the phase variation is accounted for by modes 1 and 2. In this section, we consider the impact of mesoscale currents on the phase speed of modes 1 and 2 via temporal changes in the background stratification and in the advection by the background currents. We hypothesize that the time-varying phase speed over the ridge changes the phase of $p'(-H)$ at the A2 mooring and hence the rate of barotropic to baroclinic conversion.

a. Mesoscale variability

For each 28-day window used in the tidal complex demodulation analysis, we define $\mathbf{U}(\mathbf{z})$ as the time-averaged horizontal background velocity. At the A2 and C2 moorings, two episodes of intensified background current speeds ($|\mathbf{U}| > 0.05$ m s^{-1}) occur above 400-m depth during the deployment (Fig. 6). The first episode from December to the end of February is characterized by a mean southwestward flow. The flow direction switches from west-southwestward to south-southwestward at the end of January. The second episode from March to

May is characterized by a northwestward flow. The flow direction changes from west-northwestward to north-northwestward at the end of April.

The NCOM simulations show an anticyclonic eddy of 100-km radius centered to the north of Kauai in January and February 2003 (Figs. 7a,b). The anticyclone is associated with flow toward the southwest at the KR. A cyclonic eddy of 100-km radius forms off the east side of the island of Hawaii (Fig. 7a), strengthens, and drifts westward during February and March (Figs. 7b,c). It is located south of the KR in May (Fig. 7d), causing northeastward flow at the KR.

The NCOM predictions of $\mathbf{U}(\mathbf{z})$ near the surface at the locations of the A2 and C2 moorings compares favorably with the observations (Fig. 8). This suggests that the southwestward flow observed at the two moorings from December to February is due to the anticyclonic eddy north of Kauai. The flow direction varies (Fig. 6) as the eddy propagates to the west (Fig. 7). Likewise, the northwestward flow from the end of February to May appears linked to the cyclonic eddy south of the KR. The flow direction switches (Fig. 6) as the cyclonic eddy propagates to the northwest (Fig. 7).

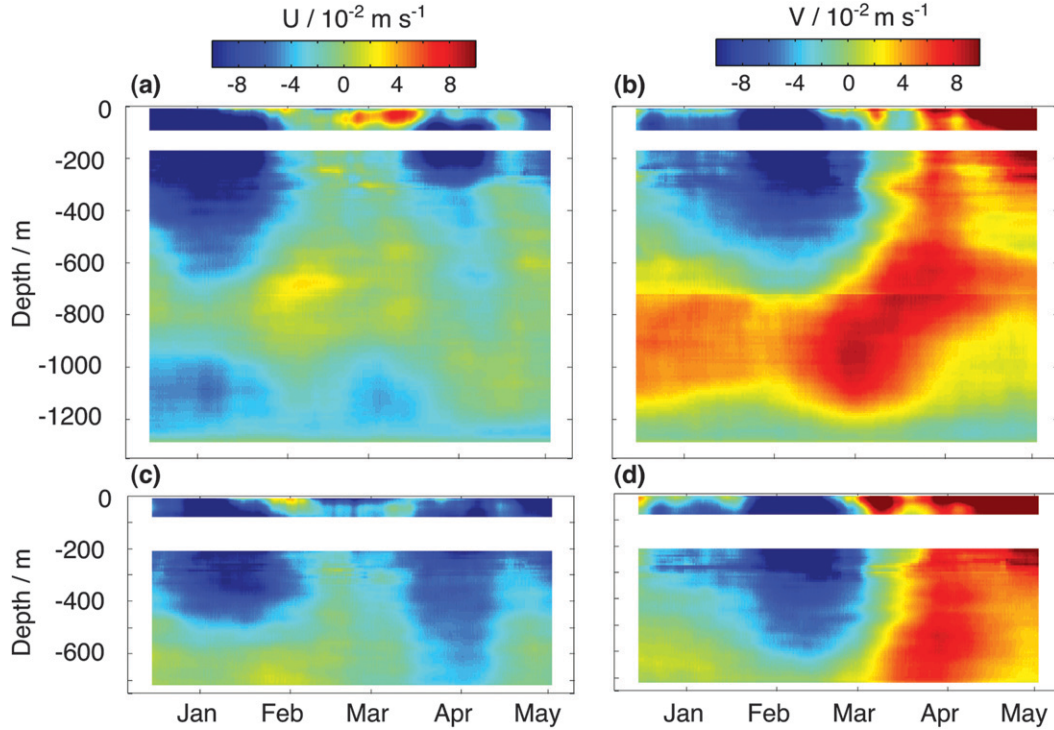The density anomaly ρ_a for each 28-day window is estimated as

FIG. 6. Mesoscale currents U and V computed at the (a),(b) A2 and (c),(d) C2 moorings.

$$\rho_a(z) = \rho_B(z) - \langle \rho_B(z) \rangle. \qquad (13)$$

Here, $\rho_B(z)$ is the density averaged over a 28-day window and $\langle \cdot \rangle$ indicates a time average over the entire deployment.

The observations above 600 m at the A2 and C2 moorings show two episodes of intensified density anomaly $[|\rho_a(z)| > 0.02 \text{ kg m}^{-3}]$ (Fig. 9). The first episode, from December to the end of February, is characterized by relatively light water $[\rho_a(z) < 0]$, consistent with the passage of an anticyclonic eddy. The second episode, from March to May, yields denser water $[\rho_a(z) > 0]$ during the passage of the cyclonic eddy.

b. Phase change of p' associated with the mesoscale variability

Variations in the phase of $p'(-H)$ at A2 strongly influence the time-variable conversion (Figs. 2a,d). We consider two possible explanations for the variable phase of $p'(-H)$ at A2. First, we examine the change in phase speed of the M_2 internal tide over the ridge due to changes in stratification. We consider the impact on the most energetic modes 1 and 2. The phase lag for an internal wave mode generated at the northern flank of the ridge to propagate to the A2 mooring is

$$\Gamma = \frac{L}{\overline{c}_n}, \qquad (14)$$

where $L = 60$ km is the distance between A2 and the main generation zone on the northern side of the ridge (Fig. 1b) and $\overline{c}_n$ is the time-averaged phase speed over the duration of the mooring deployment. Here, $\overline{c}_n$ is treated as spatially uniform over the top of the ridge.

The phase lag perturbation associated with changes in the background stratification is

$$\Delta\Gamma_n(N_B) = L\left(\frac{1}{\hat{c}_n} - \frac{1}{\overline{c}_n}\right) = \frac{\phi_n(N_B)}{\omega}, \qquad (15)$$

where $\hat{c}_n$ is the time-dependent phase speed, which is a function of the variable background stratification N_B, and $\phi_n(N_B)$ is the phase shift at A2 associated with the variable phase speed. The contribution of the background stratification to the phase of the perturbation pressure is calculated as

$$\hat{\phi}_n(N_B) = \phi_n(N_B) - \overline{\phi}_n(N_B) + \overline{\phi}_{p'_n}, \qquad (16)$$

where $\overline{\phi}_n(N_B)$ is the time-averaged $\phi_n(N_B)$ and $\overline{\phi}_{p'_n}$ is the time-averaged $\phi_{p'_n}$ over the duration of the mooring deployment.
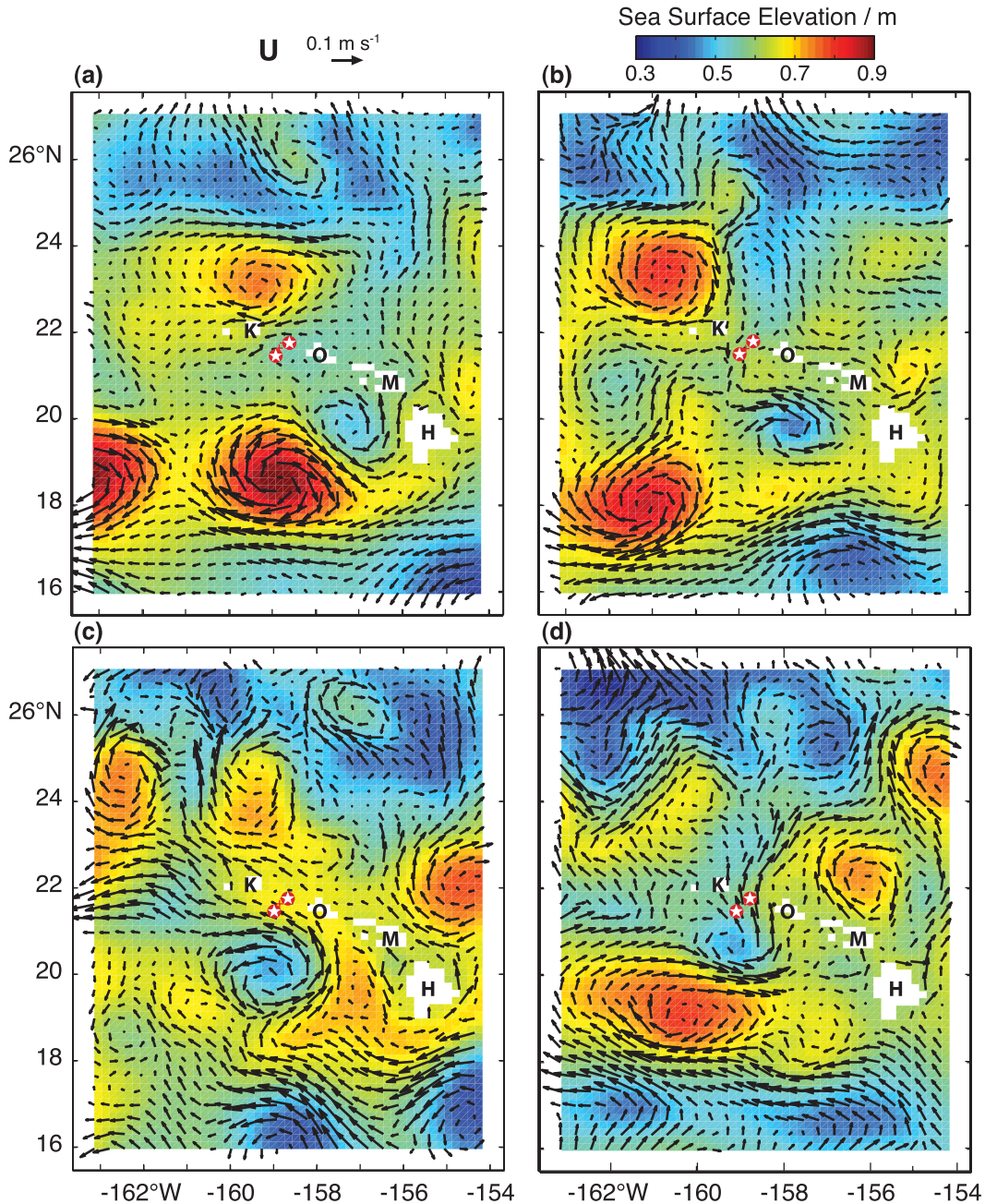
FIG. 7. Mesoscale current vectors predicted using NCOM over the Hawaiian Islands on (a) 3 Jan, (b) 8 Feb, (c) 22 Mar, and (d) 1 May 2003. The underlying color gives the sea surface elevation amplitude. The northernmost star is the location of the A2 mooring (21°45.087N, 158°45.522W), and the more southern star is the location of the C2 mooring (21°37.850N, 158°51.609W).

The second possible cause for time-varying internal wave phase speed over the ridge is time-varying advection by the background current. A cross-ridge flow, in addition to a time-dependent background stratification, alters the phase speed of mode n as measured by a stationary observer by

$$\tilde{c}_n(N_B, V_\perp) = \hat{c}_n(N_B) + V_\perp, \qquad (17)$$

where $V_\perp$ is the depth-averaged, cross-ridge (positive toward 37.4°N) current averaged over each 28-day window computed at A2 from the observations. The phase
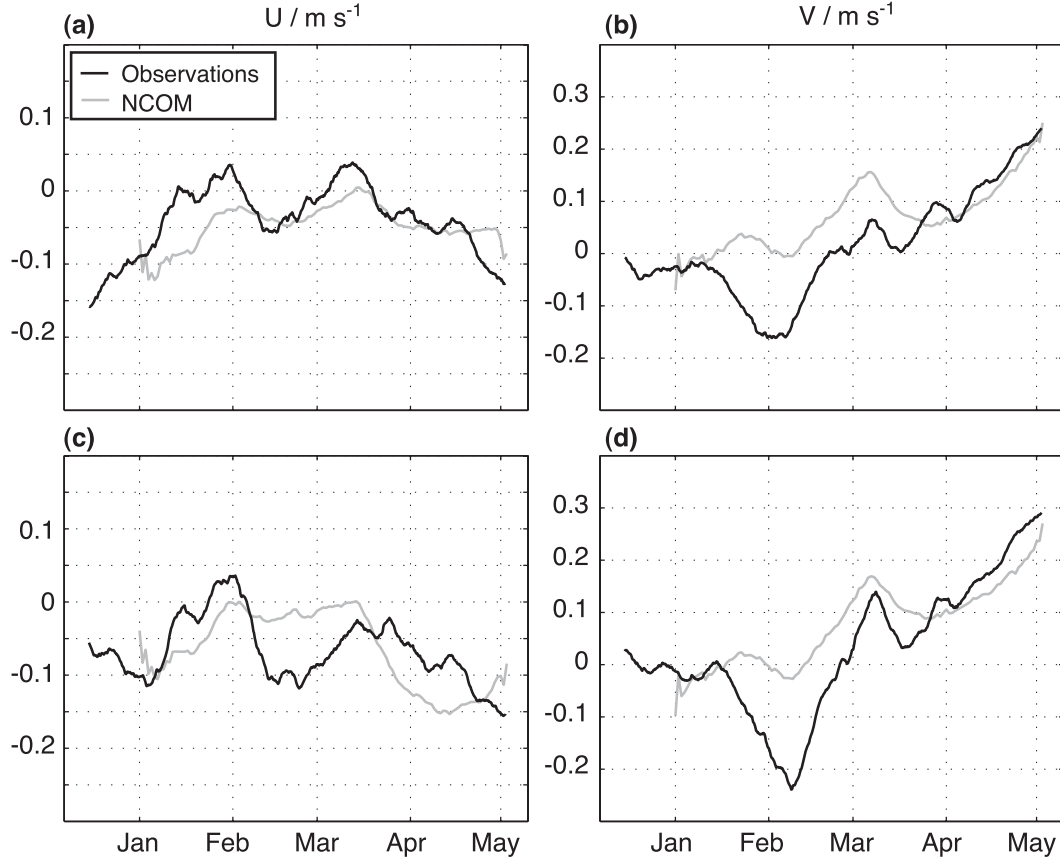
FIG. 8. Comparisons between mesoscale currents U and V amplitudes at the (a),(b) A2 and (c),(d) C2 moorings at 8-m depth and predicted using NCOM at the surface. The NCOM predictions are smoothed over 28-day windows.

lag difference induced by the background stratification and the background circulation is

$$\Delta\Gamma_n(N_B, V_\perp) = L\left(\frac{1}{\tilde{c}_n} - \frac{1}{\overline{c}_n}\right) = \frac{\phi_n(N_B, V_\perp)}{\omega}. \quad (18)$$

The contribution of the background stratification and the background circulation to the phase of the perturbation pressure is calculated as

$$\hat{\phi}_n(N_B, V_\perp) = \phi_n(N_B, V_\perp) - \overline{\phi}_n(N_B, V_\perp) + \overline{\phi}_{p'_n}, \quad (19)$$

where $\overline{\phi}_n(N_B, V_\perp)$ is the time-averaged $\phi_n(N_B, V_\perp)$ over the duration of the mooring deployment.

We compare the contribution to the energy conversion of the $p'(-H)$ phase from the observations $[\cos(\phi_{p'_n} - \phi_{\hat{w}_{bt}})]$ to the contributions of the $p'(-H)$ phase induced by the background stratification $\{\cos[\hat{\phi}_n(N_B) - \phi_{\hat{w}_{bt}}]\}$ and the $p'(-H)$ phase induced by the combination of the background stratification and background circulation $\{\cos[\hat{\phi}_n(N_B, V_\perp) - \phi_{\hat{w}_{bt}}]\}$.

The magnitude of the stratification-induced phase changes for mode 1 is similar to the observations at the beginning and at the end of the mooring deployment (Fig. 10a). However, $\cos[\hat{\phi}_1(N_B) - \phi_{\hat{w}_{bt}}]$ shows values higher than $\cos(\phi_{p'_1} - \phi_{\hat{w}_{bt}})$ in February and lower than $\cos(\phi_{p'_1} - \phi_{\hat{w}_{bt}})$ in March. Adding the estimated cross-ridge current improves the correspondence of the phase of the perturbation pressure with the observations for mode 1 (Fig. 10b). Both $\cos[\hat{\phi}_1(N_B, V_\perp) - \phi_{\hat{w}_{bt}}]$ and $\cos(\phi_{p'_1} - \phi_{\hat{w}_{bt}})$ show an increase from late January/early February to April. We suggest that the background stratification and the background circulation contribute to the time variability of the energy conversion for mode 1.

The stratification-induced phase changes for mode 2 show a close correspondence with the observations (Fig. 10c). Both $\cos[\hat{\phi}_2(N_B) - \phi_{\hat{w}_{bt}}]$ and $\cos(\phi_{p'_2} - \phi_{\hat{w}_{bt}})$ show a decrease from December to the end of January and an increase from February to the end of March. The good agreement between $\cos[\hat{\phi}_2(N_B) - \phi_{\hat{w}_{bt}}]$ and $\cos(\phi_{p'_2} - \phi_{\hat{w}_{bt}})$ suggests that the background stratification accounts for the time variability of the energy conversion for mode 2. Including the cross-ridge current overestimates the cosine of the observed phase differences (Fig. 10d).
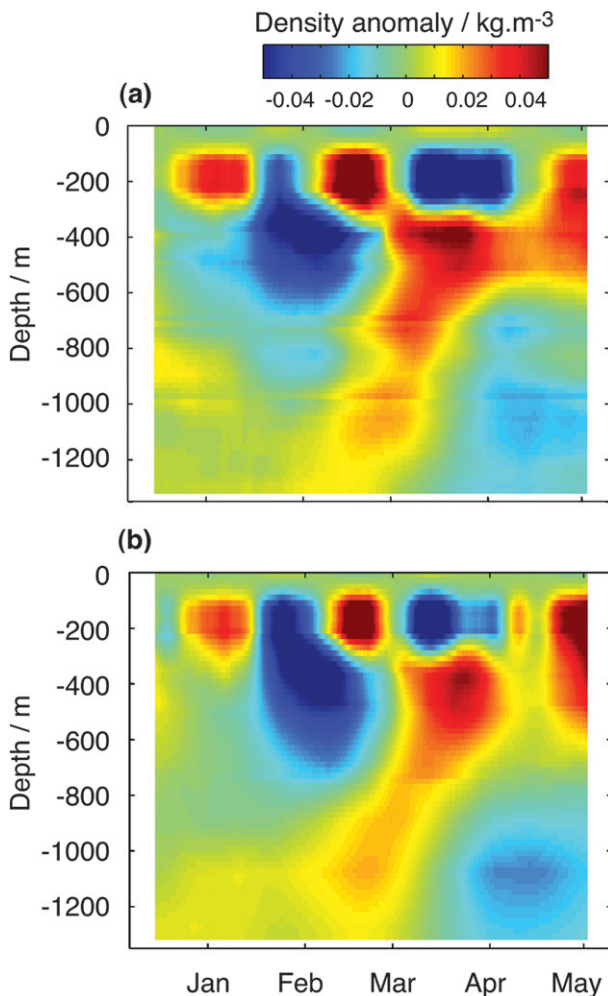
FIG. 9. Density anomaly ρ_a computed at the (a) A2 and (b) C2 moorings.

7. Summary and conclusions

In this work, we examine the time variability of the barotropic to baroclinic energy conversion and baroclinic energy fluxes for the M_2 tide obtained from observations at the Kaena Ridge between December 2002 and May 2003. The main result is the time variability found in the barotropic to baroclinic energy conversion at the A2 mooring. The observations indicate a factor of 2 change in energy conversion between the highest values in December and April and the lowest values in January and February (Fig. 2). The time variability of the energy conversion arises from the amplitude and phase of the perturbation pressure. Half of the energy conversion is accounted for by the first two baroclinic modes, and two-thirds of this amount (33% of the total) is accounted for by mode 1. The time variability of the energy conversion for modes 1 and 2 is related to the

phase changes of the perturbation pressure at the bottom (Fig. 3). The good correspondence between the time variability of the energy conversion at the A2 mooring and the amplitude of the depth-integrated baroclinic energy flux at the C2 mooring (Fig. 4) suggests that the energy conversion at the A2 mooring is representative of the energy conversion on the southern flank of the KR.

The observations at the A2 and C2 moorings reveal two episodes of intensified current (Fig. 6). Comparisons between the observations and simulations from NCOM reveal that the flows observed at both moorings correspond to an anticyclonic eddy centered to the north of Kauai followed by a cyclonic eddy centered on the southern flank of the KR. The passage of the two eddies near Kaena Ridge also result in stratification changes in the upper 1000 m of the water column (Fig. 9). Estimates of the impact of the variable stratification on the internal mode phase speeds suggest that the time variability of the energy conversion is induced by changes in the mode-2 propagation speed. The background stratification may affect mode 2 more than mode 1 because of smaller mode-2 propagation and phase speeds. The time-variable energy conversion for mode 1 is affected by the background stratification to some extent (Fig. 10). Including the estimated cross-ridge current improves the fit to mode-1 phase but does not significantly improve the fit to mode-2 phase. Given the broad assumptions that go to into this assessment (e.g., low-frequency observations at A2 represent mesoscale currents and stratification over the entire KR, neglect of internal tides generated on the south flank, and use of flat-bottom modes over sloping topography), we find these comparisons to be encouraging if not definitive. The calculations suggest that phase lag changes over the ridge account for changes in perturbation pressure phase at A2, which in turn modulates the energy conversion. Simultaneous observations of the internal tide and mesoscale fields on the flanks of the KR are needed to examine this interaction in more detail.

We note that incoherent barotropic to baroclinic tidal energy conversion for a single ridge will differ, depending on the cause of the incoherency. For example, if the background current is quasi uniform across the ridge, the flow will cause a decrease in phase lag of the internal tide in the direction of the flow and an increase in the opposite direction. This will cause the phase of the perturbation pressure to increase on one side of the ridge and decrease on the other, which may lead to no net change in the conversion integrated over the entire ridge, although the flux will be higher on one side compared to the other. In contrast, a uniform change in the background stratification will affect the conversion on
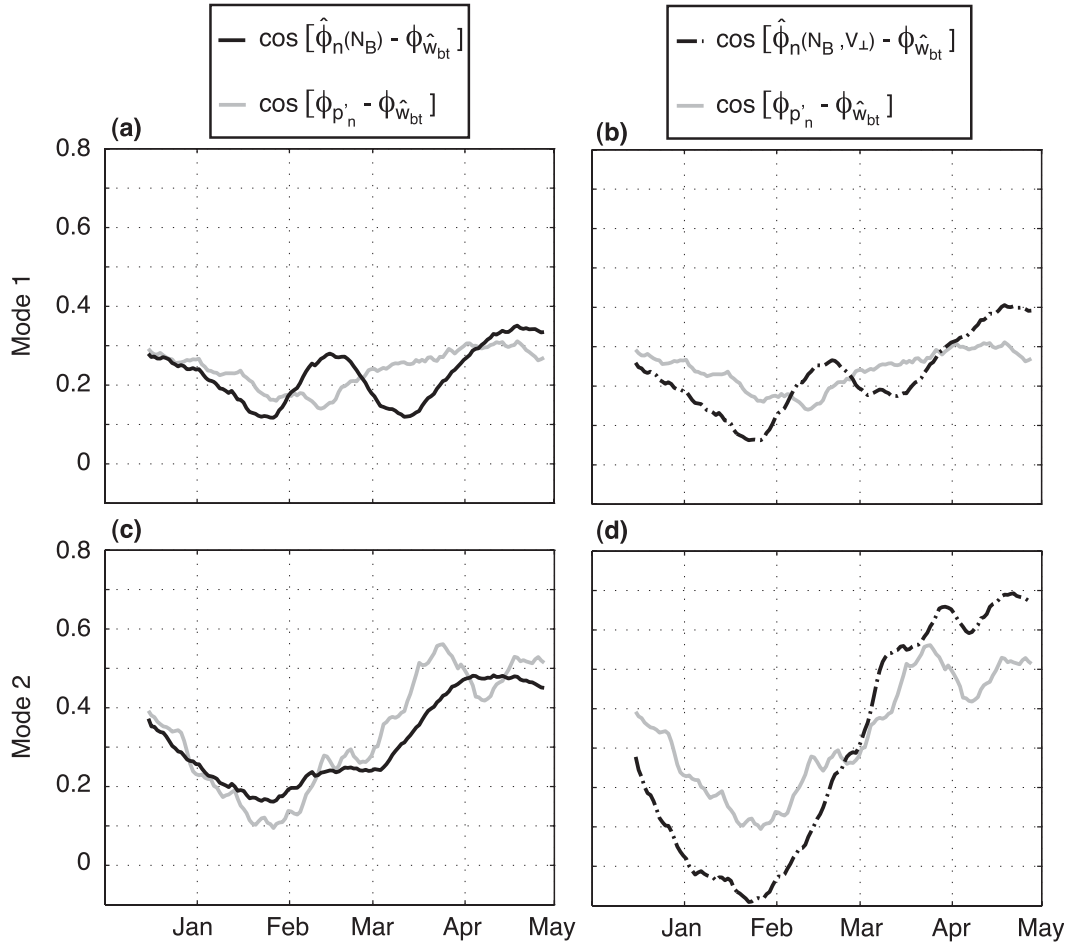
FIG. 10. Comparison between the time series of the contributions to the energy conversion of the phase of the perturbation pressure induced by the background stratification $\cos[\hat{\phi}_n(N_B) - \phi_{\hat{w}_{bt}}]$ and from the observations $\cos(\phi_{p'_n} - \phi_{\hat{w}_{bt}})$ and comparison between the contributions of the phase of the perturbation pressure induced by the background stratification and the background circulation $\cos[\hat{\phi}_n(N_B, V_\perp) - \phi_{\hat{w}_{bt}}]$ and from the observations $\cos(\phi_{p'_n} - \phi_{\hat{w}_{bt}})$, for (a),(b) mode 1 and (c),(d) mode 2 at the A2 mooring. The correlation between $\cos(\phi_{p'_n} - \phi_{\hat{w}_{bt}})$, and $\cos[\hat{\phi}_n(N_B) - \phi_{\hat{w}_{bt}}]$ is 0.44 for mode 1 and 0.93 for mode 2. Adding the cross-ridge improves the fit to mode 1 {correlation between $\cos(\phi_{p'_n} - \phi_{\hat{w}_{bt}})$, and $\cos[\hat{\phi}_n(N_B, V_\perp) - \phi_{\hat{w}_{bt}}]$ is 0.64} but does not significantly improve the fit to mode 2 {correlation between $\cos(\phi_{p'_n} - \phi_{\hat{w}_{bt}})$, and $\cos[\hat{\phi}_n(N_B, V_\perp) - \phi_{\hat{w}_{bt}}]$ is 0.95}.

either side of the ridge, as well as the phase lag of the generated internal tides over the top of the ridge, in the same sense, thus changing the net conversion for the ridge.

Our findings are complementary to those of Kelly and Nash (2010), who documented variable tidal conversion on the New Jersey shelf due to the shoaling of internal tides from offshore. The present study differs in that the presence of offshore, random internal tides is not considered. Instead, we focus on the variability of the locally generated internal tide due to the effects of a variable mesoscale circulation. This study thus concerns the variability of the otherwise phase-locked or coherent internal tide as the wave is generated, taking into account that the generation site is taken as the ridge topography as a whole rather than a single flank of the ridge.

REFERENCES

Alford, M. H., J. A. MacKinnon, Z. Zhao, R. Pinkel, J. Klymak, and T. Peacock, 2007: Internal waves across the Pacific. *Geophys. Res. Lett.,* **34,** L24601, doi:10.1029/2007GL031566.

Barron, C. N., A. B. Kara, P. J. Martin, R. C. Rhodes, and L. F. Smedstad, 2006: Formulation, implementation and examination of vertical coordinate choices in the global Navy Coastal Ocean Model (NCOM). *Ocean Modell.,* **11,** 347–375.

Blumberg, A. F., and G. L. Mellor, 1987: A description of a three-dimensional coastal ocean circulation model. *Three-Dimensional Coastal Ocean Models,* N. S. Heaps, Ed., Coastal and Estuarine Sciences, Vol. 4, Amer. Geophys. Union, 1–16.

Boyd, T. J., M. D. Levine, S. R. Gard, and W. Waldorf, 2005: Mooring observations from the Hawaiian Ridge. Oregon State University College of Oceanic and Atmospheric Sciences Data Rep. 197, 232 pp.

Carter, G. S., and M. A. Merrifield, 2007: Open boundary conditions for regional tidal simulations. *Ocean Modell.,* **18,** 194–209.

——, ——, J. Becker, K. Katsumata, M. C. Gregg, and Y. L. Firing, 2008: Energetics of M_2 barotropic to baroclinic tidal conversion at the Hawaiian Islands. *J. Phys. Oceanogr.,* **38,** 2205–2223.

Chavanne, C., P. Flament, G. Carter, M. Merrifield, D. Luther, E. Zaron, and K.-W. Gurgel, 2010a: The surface expression of semi-diurnal internal tides in the Kauai Channel, Hawaii. Part I: Observations and numerical predictions. *J. Phys. Oceanogr.,* **40,** 1155–1179.

——, ——, D. Luther, and K.-W. Gurgel, 2010b: The surface expression of semi-diurnal internal tides in the Kauai Channel, Hawaii. Part II: Interactions with mesoscale currents. *J. Phys. Oceanogr.,* **40,** 1180–1200.

Chelton, D. B., R. A. deSzoeke, M. G. Schlax, K. E. Naggar, and N. Siwertz, 1998: Geographical variability of the first baroclinic Rossby radius of deformation. *J. Phys. Oceanogr.,* **28,** 433–460.

Chiswell, S. M., 2002: Energy levels, phase and amplitude modulation of the baroclinic tide off Hawaii. *J. Phys. Oceanogr.,* **32,** 2640–2651.

Cole, S. T., D. L. Rudnick, B. A. Hodges, and J. P. Martin, 2009: Observations of tidal internal wave beams at Kauai Channel, Hawaii. *J. Phys. Oceanogr.,* **39,** 421–436.

Egbert, G. D., and S. Y. Erofeeva, 2002: Efficient inverse modeling of barotropic ocean tides. *J. Atmos. Oceanic Technol.,* **19,** 183–204.

——, A. F. Bennet, and M. G. Foreman, 1994: TOPEX/Poseidon tides estimated using a global inverse model. *J. Geophys. Res.,* **99,** 24 821–24 852.

Eich, M. L., M. A. Merrifield, and M. H. Alford, 2004: Structure and variability of semidiurnal internal tides in Mamala Bay, Hawaii. *J. Geophys. Res.,* **109,** C05010, doi:10.1029/2003JC002049.

Emery, W. J., and R. E. Thomson, 2001: *Data Analysis Methods in Physical Oceanography.* Elsevier, 638 pp.

Fofonoff, P., and R. C. Millard, 1983: Algorithms for computation of fundamental properties of seawater. UNESCO Tech. Papers in Marine Science 44, 58 pp.

Jayne, S. R., and L. C. St. Laurent, 2001: Parameterizing tidal dissipation over rough topography. *Geophys. Res. Lett.,* **28,** 811–814.

Karl, D. L., F. Tupas, F. Santiago-Mandujano, C. Nosse, D. Hebel, E. Firing, and R. Lukas, 1996: Hawaiian Ocean Time-series program: Data report 7: 1995. University of Hawaii School of Ocean and Earth Science and Technology Tech. Rep. 96-09, 228 pp.

Kelly, S. M., and J. D. Nash, 2010: Internal-tide generation and destruction by shoaling internal tides. *Geophys. Res. Lett.,* **37,** L23611, doi:10.1029/2010GL045598.

Kennan, S. C., and R. Lukas, 1996: Saline intrusions in the intermediate waters north of Oahu, Hawaii. *Deep-Sea Res.,* **43,** 215–241.

Kunze, E., L. K. Rosenfeld, G. S. Carter, and M. C. Gregg, 2002: Internal waves in Monterey Submarine Canyon. *J. Phys. Oceanogr.,* **32,** 1890–1913.

Lee, C. M., E. Kunze, T. B. Sanford, J. D. Nash, M. A. Merrifield, and P. E. Holloway, 2006: Internal tides and turbulence along the 3000-m isobath of the Hawaiian ridge. *J. Phys. Oceanogr.,* **36,** 1165–1583.

Martin, J. P., D. L. Rudnick, and R. Pinkel, 2006: Spatially broad observations of internal waves in the upper ocean at the Hawaiian Ridge. *J. Phys. Oceanogr.,* **36,** 1085–1103.

Mellor, G. L., and T. Yamada, 1982: Development of a turbulence closure model for geophysical fluid problems. *Rev. Geophys. Space Phys.,* **20,** 851–875.

Merrifield, M. A., and P. E. Holloway, 2002: Model estimates of M_2 internal tide energetics at the Hawaiian Ridge. *J. Geophys. Res.,* **107,** 3179, doi:10.1029/2001JC000996.

Mitchum, G. T., and S. M. Chiswell, 2000: Coherence of the internal tide variations along the Hawaiian Ridge. *J. Geophys. Res.,* **105,** 653–661.

Nash, J. D., E. Kunze, C. M. Lee, and T. B. Sanford, 2006: Structure of the baroclinic tide generated at Kaena Ridge, Hawaii. *J. Phys. Oceanogr.,* **36,** 1123–1135.

Rainville, L., and R. Pinkel, 2006a: Baroclinic energy flux at the Hawaiian Ridge: Observations from the R/P *FLIP. J. Phys. Oceanogr.,* **36,** 1104–1122.

——, and ——, 2006b: Propagation of low-mode internal waves through the ocean. *J. Phys. Oceanogr.,* **36,** 1220–1236.

——, S. T. M. Johnston, G. S. Carter, M. A. Merrifield, R. Pinkel, P. W. Worcester, and B. D. Dushaw, 2010: Interference pattern and propagation of the M_2 internal tide south of the Hawaiian Ridge. *J. Phys. Oceanogr.,* **40,** 311–325.

Ray, R. D., and G. T. Mitchum, 1998: Surface manifestation of internal tides in the deep ocean: Observations from altimetry and island gauges. *Prog. Oceanogr.,* **40,** 135–162.

Simmons, H. L., S. R. Jayne, L. St. Laurent, and A. Weaver, 2004: Tidally driven mixing in a numerical model of the ocean general circulation. *Ocean Modell.,* **6,** 245–263.

Wunsch, C., 1975: Internal tides in the ocean. *Rev. Geophys. Space Phys.,* **13,** 167–182.

Zaron, E. D., and G. D. Egbert, 2006: Estimating open-ocean barotropic tidal dissipation: The Hawaiian Ridge. *J. Phys. Oceanogr.,* **36,** 1019–1035.

——, C. Chavanne, G. D. Egbert, and P. Flament, 2009: Baroclinic tidal generation in the Kauai Channel inferred from high-frequency radio Doppler current meters. *Dyn. Atmos. Oceans,* **48,** 93–120.

Zilberman, N. V., J. M. Becker, M. A. Merrifield, and G. S. Carter, 2009: Model estimates of M_2 internal tide generation over Mid-Atlantic Ridge topography. *J. Phys. Oceanogr.,* **39,** 2635–2651.